where the hypothesis No. 1 was used and it was assumed that the axial gradients of shear stress and pressure are much smaller than the radial ones as an approximation which can commonly be used in the boudary layer. The energy conservation law can be written as

$$u_z \frac{\partial T}{\partial z} + u_r \frac{\partial T}{\partial r} = \frac{K}{c_p \rho} \left(\frac{\partial^2 T}{\partial r^2} + \frac{1}{r} \frac{\partial T}{\partial r} \right)$$

where it was assumed that the effect of viscous dissipation can be ignored as compared with the convective heat transfer coming from flame. Assuming that Prandtl number is 1 (hypothesis No. 2), Reynolds analogy can be used and the temperature distribution can be related to the velocity distribution in the boundary layer. Thus, one can consider the radial distribution of u_z to be similar to that of T in the boundary layer. This similarity can be expressed as follows:

$$\frac{du_z}{u_{z_b} - u_z} = \frac{dT}{T_b - T} \,. \tag{2}$$

Then, the heat flux to the wall can be linked with the shear force stress at the wall because the axial temperature differential at the wall is proportional to the heat flux to the wall and the velocity axial differential is proportional to the shear stress at the wall. The difference between the scales of the axial and radial differentials yields the following approximations:

$$du_z \approx \frac{\tau_{rz}}{\mu} \, dr \,; \quad dT \approx -\frac{q_r}{K} \, dr \,. \tag{3}$$

Equations (2) and (3) yield

$$h \equiv -\frac{q_{r_w}}{T_b - T_w} = \frac{c_p \tau_{r z_w}}{u_{z_b}} \,. \tag{4}$$

From the definition of Stanton numbers and Eq. (4), the following equation can be derived:

$$C_H \equiv \frac{h}{c_p \rho u_b} = \frac{\tau_{r z_w}}{\rho_b u_b} \,.$$

For the sake of convenience in subsequent calculations, the nondimensional axial skin-friction parameter can be defined that is called "axial skin-friction coefficient"

$$\frac{c_{fz}}{2} \equiv -\frac{\tau_{r z_w}}{\rho_e u_{z_e}^2} \left(= -\frac{\tau_{z_w}}{\rho_e u_{z_e}^2} \right) \tag{5}$$

where the minus sign is put to show that the shear stress at the wall is always opposit to the flow direction. Therefore, the heat flux to the wall can be written as

$$\dot{Q}_c = C_H \rho_b u_b \Delta h = \frac{c_{f_z}}{2} \frac{\rho_e u_{z_e}^2}{u_{b_z}} \Delta h \,. \tag{6}$$

Let us focus on the right-hand side of Eq. (6). In this expression, there is no variable related to circumferential components. Considering the fact that the circumferential energy balance is zero because of the axisymmetric flow, this result is reasonable. Then, one can expect that the axial friction coefficient should be affected only by swirl because of the hypothesis of Marxman *et al.* [12]. Therefore, in the next section, an attempt is made to express the axial skin-friction coefficient through the axial distance, mass flux, swirl number, scale of the motor, and other variables known in advance.

3.2 Turbulent Flow Models

Next, let us express the axial skin-friction coefficient through other parameters that can be known in advance. The first of three different turbulent stress models is the Prandtl's mixing length theory extended to three dimensions by Czernuszenko and Rylov [13]. If each eigenvector of the mixing length tensor is parallel to each cylinder coordinate axis and all norms of the eigenvectors are the same, the axial component of the shear stress including Reynolds stress is expressed as

$$\tau_{rz} \approx \left\{ \mu + \rho l^2 \left(\left| \frac{\partial \overline{u}_\theta}{\partial r} - \frac{\overline{u}_\theta}{r} \right| + \left| \frac{\partial \overline{u}_z}{\partial r} \right| \right) \right\} \frac{\partial \overline{u}_z}{\partial r} \tag{7}$$

where the circumferential partial differentials are assumed to be much larger than the axial ones.

The second one comes from the expression in the boundary layer theory for the evaporating surface of flat plate in 2D coordinates extended by Dorance and Dore [14] to the 3D axisymmetric flows:

$$\tau_{rz} \approx \tau_{rz_w} \left(1 + B_z \varphi_z\right) ; \tag{8}$$

$$\tau_{r\theta} \approx \tau_{r\theta_w} \left(1 + B_\theta \varphi_\theta\right) \tag{9}$$

where the boundary layer thickness is assumed to be much thinner than the port radius. The definitions of B_z and B_θ are

$$B_z \equiv \frac{(\rho u_r)_w u_{z_e}}{\tau_{z_w}} ; \quad B_\theta \equiv \frac{(\rho u_r)_w u_{\theta_e}}{\tau_{\theta_w}} .$$

Equations (8) and (9) are derived by evaluating the Reynolds stress and blowing factor in the same way as it is made for the flat plate. Note that B_z is

constant throughout the fuel port while B_θ is not. The reason for this treatment is discussed below in subsection 3.6.

So far, two of three turbulent models have been already introduced. From now on, let us use these equations for evaluating the velocity distribution and the axial skin-friction coefficient. Combining Eq. (7) with Eq. (8) yields

$$\tau_{rz_w}\,(1+B_z\varphi_z)=\left\{\mu+\rho l^2\left(\left|\frac{\partial\overline{u}_\theta}{\partial r}-\frac{\overline{u}_\theta}{r}\right|+\left|\frac{\partial\overline{u}_z}{\partial r}\right|\right)\right\}\frac{\partial\overline{u}_z}{\partial r}\,. \tag{10}$$

Here, the power law in cases of no fuel vaporization (hypotheses Nos. 6 and 7) is written as

$$\varphi_z=\eta_z^{n_z}\,;\qquad \overline{\omega}=\eta_\theta^{n_\theta} \tag{11}$$

where $n_z=n_\theta=1/7$ is set.

Applying Eqs. (11) to the absolute values of the velocity partial differentials in Eq. (10) yields

$$\begin{aligned}\frac{c_{f_z}}{2}\,\frac{u_{z_e}(R-\delta_\theta)}{\kappa^2 n_\theta\delta_z u_{\theta_e}}\,(1+B_z\varphi_z)\\ =\left\{\eta_z^2-\frac{R-\delta_\theta}{\delta_z}\left(1+\frac{n_z u_{z_e}}{n_\theta u_{\theta_e}}\right)\eta_z-\frac{u_{z_e}(R-\delta_\theta)}{\kappa^2\mathrm{Re}_{\delta_z}n_\theta\delta_z u_{\theta_e}}\right\}\frac{\partial\varphi_z}{\partial\eta_z}\end{aligned} \tag{12}$$

where $l=\kappa(R-r)$ and $\kappa=0.4$.

Equation (12) can be integrated in the radial direction from the edge of the boudary layer to the fuel port wall. This integration yields

$$\frac{c_{f_z}}{2}\approx\frac{\kappa^2(n_\theta u_{\theta_e}/u_{z_e}+n_z)}{\ln\left(1+\kappa^2\mathrm{Re}_{\delta_z}(n_\theta u_{\theta_e}/u_{z_e}+n_z)\right)}\,\frac{\ln(1+B_z)}{B_z} \tag{13}$$

where the approximations $R\gg\delta_z,\delta_\theta$ and $\kappa^2\mathrm{Re}_{\delta_z}n_\theta\gg 1$ are used. The first term in the right-hand side of Eq. (13) can be approximated in the easier way as

$$\frac{c_{f_z}}{2}=(\alpha_z\xi+\beta_z)\,\mathrm{Re}_{\delta_z}^{\gamma_z}\,\frac{\ln(1+B_z)}{B_z} \tag{14}$$

where $(\alpha_z,\beta_z,\gamma_z)=(0.00769,0.0233,-0.125)$ is set. Let us refer $\xi\equiv u_{\theta_e}/u_{z_e}$ to as the "swirl strength." If $\xi=0$, Eq. (14) becomes the same as Marxman's approximation [6].

Though the axial skin-friction coefficient has been written as Eq. (14) through the variables descibing the flow properties, in Eq. (14), there are three variables that cannot be easily determined: ξ, u_{z_e}, and δ_z. Therefore, three additional constraints are necessary.

The first one is the Boussinesq approximation, which is the third of the three turbulent models:

$$\tau_{rz} = \frac{(\mu + \rho\varepsilon)u_{z_e}}{\delta_z} \frac{\partial \varphi_z}{\partial \eta_z} ; \tag{15}$$

$$\tau_{r\theta} = (\mu + \rho\varepsilon) \frac{u_{\theta_e}}{\delta_\theta} \frac{\partial \varphi_\theta}{\partial \eta_\theta} . \tag{16}$$

Applying Eqs. (15) and (16) to Eqs. (8) and (9) yields

$$\frac{\tau_{rz_w}\delta_z}{(\mu + \rho\varepsilon)u_{z_e}} (1 + B_z\varphi_z) = \frac{\partial \varphi_z}{\partial \eta_z} ; \tag{17}$$

$$\frac{\tau_{r\theta_w}\delta_\theta}{(\mu + \rho\varepsilon)u_{\theta_e}} (1 + B_\theta\varphi_\theta) = \frac{\partial \varphi_\theta}{\partial \eta_\theta} . \tag{18}$$

It is assumed here that $\tau_{rz_w}\delta_z/((\mu+\rho\varepsilon)u_{z_e})$ consists of the product of two single-variable functions of η_z and B_z just in the same way as in Marxman's [5]. In the cases of no blowing, Eqs. (17) and (18) are equivalent to the derivative-type of Eqs. (11). Moreover, one can use the approximation:

$$1 + B_z\varphi_z \approx 1 + B_z\eta_z^{n_z}$$

because of the hypothesis No. 6. Therefore, Eq. (17) can be expressed as

$$\frac{\partial \varphi_z}{\partial \eta_z} = F(B_z)n_z\eta_z^{n_z-1} (1 + B_z\eta_z^{n_z}) . \tag{19}$$

Equation (19) can be now integrated in the radial direction from the edge of the boudary layer to the fuel port wall. Applying the boundary conditions $\varphi_z(\eta_z = 0) = 0$ and $\varphi_z(\eta_z = 1) = 1$ leads to

$$\varphi_z = \frac{\eta_z^{n_z} (1 + (B_z/2)\eta_z^{n_z})}{1 + B_z/2} . \tag{20}$$

As for the circumferential direction, similar to the derivation of Eq. (20), one can derive

$$\overline{\omega} = \frac{\eta_\theta^{n_\theta} (1 + (B_\theta/2)\eta_\theta^{n_\theta})}{1 + B_\theta/2} \tag{21}$$

where $R \gg \delta_z, \delta_\theta$ is assumed.

Now, the velocity fields have been evaluated for the radial direction in the boundary layer. These equations are used in two situations. One of them is the case when one compares shear stresses with and without fuel blowing. Another is the case when Eqs. (14), (20), and (21) are combined to obtain the Karman's momentum integral equation and the axial skin-friction coefficient is derived as a function of axial position.

3.3 Karman's Momentum Integral Equation

Let us now derive the Karman's momentum integral equation in the axisymmetric pipe flow as the second condition for eliminating an unknown variable in Eq. (14). The mass conservation and the momentum conservation laws read:

– mass conservation law

$$\frac{\partial u_z}{\partial z} + \frac{\partial u_r}{\partial r} + \frac{u_r}{r} = 0\,; \tag{22}$$

– momentum conservation law

$$u_z \frac{\partial u_z}{\partial z} + u_r \frac{\partial u_z}{\partial r} = -\frac{1}{\rho}\frac{\partial P}{\partial z} + v\left(\frac{\partial^2 u_z}{\partial r^2} + \frac{1}{2}\frac{\partial u_z}{\partial r}\right)\,; \tag{23}$$

$$\frac{u_\theta^2}{r} = -\frac{1}{\rho}\frac{\partial P}{\partial r}\,; \tag{24}$$

$$u_z \frac{\partial u_\theta}{\partial z} + u_r \frac{\partial u_\theta}{\partial r} + \frac{u_r u_\theta}{r} = v\left(\frac{\partial^2 u_\theta}{\partial r^2} + \frac{1}{r}\frac{\partial u_\theta}{\partial r} - \frac{u_\theta}{r^2}\right)\,.$$

where axial partial differentials were ignored in viscous terms.

Equation (22) multiplied by zu_z plus Eq. (23) multiplied by r and the partial integration of Eq. (19) yield the momentum integral equation

$$\frac{\partial}{\partial z}\int_R^{R-\delta_z} r u_z^2\,dr - u_{z_e}\frac{\partial}{\partial z}\int_R^{R-\delta_z} r u_z\,dr = -\frac{R\tau_{rz_w}}{\rho}(1+B_z) - \frac{\partial}{\partial z}\int_R^{R-\delta_z}\frac{rP}{\rho}\,dr \tag{25}$$

where $(\rho u_r)_w$ must be considered as a nonzero variable. Contrary to axial flows, $\partial P/\partial r$ is approximated as 0 at the edge of boundary layer; in swirl flows, this assumption cannot be used because of Eq. (24). Thus, one should consider how to evaluate the pressure gradient $(\partial/\partial z)(rP/\rho)$. Now, the pressure in the boundary layer can be expressed as

$$P(z,r) = P(z,R-\delta_z) + \int_{R-\delta_z}^{r}\left.\frac{\partial P}{\partial r}\right|_z dr = P(z,R-\delta_z) - \int_{R-\delta_z}^{r}\rho\frac{u_\theta^2}{r}\,dr\,. \tag{26}$$

Applying Eq. (26) to the second term in the right-hand side of Eq. (25) leads to

$$\frac{\partial}{\partial z}\int_R^{R-\delta_z}\frac{rP}{\rho}\,dr = \int_R^{R-\delta_z} r\left(\frac{1}{\rho}\left.\frac{\partial P}{\partial z}\right|_{R-\delta_z} - \frac{\partial}{\partial z}\int_{R-\delta_z}^{r}\frac{u_\theta^2}{r}\,dr\right)dr\,. \tag{27}$$

The hypothesis No. 4 and Eq. (25) yield for the edge of the boundary layer:

$$\left.\frac{\partial P}{\partial z}\right|_{R-\delta_z} = 0\,. \tag{28}$$

Because of hypothesis No. 9, one can divide the last term of Eq. (27) and evaluate it as

$$\begin{aligned}
-\int_R^{R-\delta_z}\left(r\,\frac{\partial}{\partial z}\int_{R-\delta_z}^{r}\frac{u_\theta^2}{r}\,dr\right)dr &= -\frac{\partial}{\partial z}\int_{R-\delta_\theta}^{R-\delta_z} r\left(\int_{R-\delta_z}^{r}\frac{u_\theta^2}{r}\,dr\right)dr \\
&\quad -\frac{\partial}{\partial z}\int_R^{R-\delta_z} r\left(\int_{R-\delta_z}^{R-\delta_\theta}\frac{u_\theta^2}{r}\,dr\right)dr - \frac{\partial}{\partial z}\int_R^{R-\delta_\theta} r\left(\int_{R-\delta_\theta}^{r}\frac{u_\theta^2}{r}\,dr\right)dr \\
&\approx \frac{1}{2}\,\frac{\partial}{\partial z}\left\{R^2\omega_e^2\left(\delta_z^2-\delta_\theta^2\right)\right\} + \frac{\partial}{\partial z}\left\{\frac{49(170B_\theta^2+792B_\theta+935)R^2\omega_e^2\delta_\theta^2}{33{,}660(B_\theta+2)^2}\right\}
\end{aligned} \tag{29}$$

where the last expression is an approximated form of the first and the second expressions when only the largest scale terms ($\partial R^2\delta^2/\partial z$) are left. Applying Eqs. (28) and (29) to Eq. (25) and nondimensionalizing it, one obtains:

$$\begin{aligned}
\frac{7(40B_z^2+143B_z+110)}{1980(B_z+2)^2}\,\frac{\partial\delta_z}{\partial z} &\approx \frac{c_{f_z}}{2}\,(1+B_z) \\
&\quad + \frac{1}{2}\,\frac{\partial}{\partial z}\left\{\xi^2\,\frac{\delta_z^2-\delta_\theta^2}{R(1-\delta_\theta/R)^2}\right\} + \frac{\partial}{\partial z}\left\{\frac{49(170B_\theta^2+792B_\theta+935)\xi^2\delta_\theta^2}{33{,}660(B_\theta+2)^2R(1-\delta_\theta/R)^2}\right\}.
\end{aligned} \tag{30}$$

Because the order of magnitude of the last two terms in the right-hand side of Eq. (30) is $\delta^2/(RL)$ which is much smaller than the one in the right-hand side (δ/L), one can approximate Eq. (30) as

$$\frac{7(40B_z^2+143B_z+110)}{1980(B_z+2)^2}\,\frac{\partial\delta_z}{\partial z} \approx \frac{c_{f_z}}{2}\,(1+B_z)\,. \tag{31}$$

This is the Karman's momentum integral equation in the 3D axisymmetric coordinates. This equation is the last one of the four models related to boundary layers.

3.4 Estimation of the Axial Skin-Friction Coefficient in Swirl Flows with No Blowing

The aim of this subsection is to show the last of three conditions needed to evaluate the axial skin-friction coefficient. Also, an attempt will be made to evaluate this coefficient in swirl and axial flows without blowing.

Before the last condition related to swirl decay will be introduced, let us define the indicator which shows the swirl strength. The swirl number is a way to express the swirl strength as:

$$S \equiv \frac{2}{R^3 u_{z_e}^2} \int_0^R r^2 u_z u_\theta \, dr \, .$$

Considering the hypotheses Nos. 4 and 5 and ignoring boundary layers, rough calculation yields

$$S \approx \frac{\xi}{2} \, .$$

Here, ξ is called "swirl strength." The last condition is the hypothesis No. 8 with the mathematical manifestation as

$$S \approx S_0 \exp(pz) \;\text{ or }\; \xi \approx \xi_0 \exp(pz) \tag{32}$$

where $p = -0.569 \mathrm{Re}_D^{-0.277}/D$. These equations are empirically derived from Kito *et al.* [8] and Steenbergen [9].

Now, necessary and sufficient conditions have been assembled which are Eqs. (20), (21), (31), and (32), to rewrite Eq. (14) as a single-variable function of axial direction. Next, let us compare and evaluate c_{f_z} for the case without blowing and swirling, namely, evaluate c_{f_z} as

$$\left.\frac{c_{f_z}}{2}\right|_{B_z,\xi_0} = \frac{c_{f_z}|_{B_z,\xi_0}}{c_{f_z}|_{B_z=0,\xi_0}} \, \frac{c_{f_z}|_{B_z=0,\xi_0}}{c_{f_z}|_{B_z=0,\xi_0=0}} \, \left.\frac{c_{f_z}}{2}\right|_{B_z=0,\xi_0=0} \tag{33}$$

where $(c_{f_z}/2)|_{B_z=0,\xi_0=0}$ is equivalent to $c_f/2$ in the cases of 2D flat plate and $c_f/2$ follows a famous empirical rule:

$$\frac{c_f}{2} = 0.03 \mathrm{Re}_z^{-0.2} \, . \tag{34}$$

In this subsection, $c_{f_z}|_{B_z=0,\xi_0}/c_{f_z}|_{B_z=0,\xi_0=0}$ will be evaluated for the initial swirl strength and axial direction. Now, for the cases without blowing, substituting Eqs. (14) and (32) into Eq. (31) and integration of Eq. (31) in the axial direction from 0 to z yield

$$\overline{\delta}_z|_{B_z=0} = \left\{ \frac{72(1-\gamma_z)}{7} \right\}^{1/(1-\gamma_z)} \mathrm{Re}_D \left(\alpha_z \xi_0 \, \frac{\exp(\overline{p}\,\overline{z}) - 1}{\overline{p}} + \beta_z \overline{z} \right)^{1/(1-\gamma_z)} \tag{35}$$

where the bar means that the variable is nondimensionalized by the port diameter. By substituting Eq. (35) into Eq. (31) and dividing Eq. (31) with swirl by the one without swirl, one obtains

$$\frac{c_{f_z}|_{B_z=0,\xi_0}}{c_{f_z}|_{B_z=0,\xi_0=0}} = \frac{c_{f_z}/2|_{B_z=0,\xi_0}}{c_f/2}$$
$$= \left(\frac{\alpha_z}{\beta_z}\,\xi_0\,\frac{\exp(\overline{p}\,\overline{z})-1}{\overline{p}\,\overline{z}}+1\right)^{1/(1-\gamma_z)}\left(\frac{\alpha_z}{\beta_z}\,\xi_0\exp(\overline{p}\,\overline{z})+1\right). \quad (36)$$

Equation (36) shows the relation between the axial skin-friction coefficient with swirl but without fuel blowing. This evaluation is used in the next subsections.

3.5 Estimation of the Axial Friction Coefficient in Swirl Flows with Blowing

In this subsection, let us start from comparing shear stresses with and without fuel blowing. Then, let us express the boundary layer thickness and the axial skin-friction coefficient through the fuel blowing and axial blowing parameter.

First of all, let us write the shear stress at the wall with fuel blowing as

$$\tau_{rz_w}|_{B_z} = \mu\,\frac{u_{z_e}}{\delta_z|_{B_z}}\left.\frac{\partial\varphi_z}{\partial\eta_z}\right|_w. \quad (37)$$

Near the wall, nondimensional axial velocity is approximated as follows:

$$\varphi_z = \frac{\eta_z^{n_z}\,(1+(B_z/2)\,\eta_z^{n_z})}{1+B_z/2} \approx \frac{\eta_z^{n_z}}{1+B_z/2}. \quad (38)$$

Substituting Eq. (38) into Eq. (37) yields

$$\tau_{rz_w}|_{B_z} \approx \frac{\mu}{1+B_z/2}\,\frac{u_{z_e}}{\delta_z|_{B_z}}\left.\frac{\partial\eta_z^{n_z}}{\partial\eta_z}\right|_w = \frac{1}{1+B_z/2}\,\frac{\delta_z|_{B_z=0}}{\delta_z|_{B_z}}\;\tau_{rz_w}|_{B_z=0}. \quad (39)$$

Therefore, Eq. (39) can be nondimensionalized as

$$\left.\frac{c_{f_z}}{2}\right|_{B_z} = \frac{1}{1+B_z/2}\,\frac{\delta_z|_{B_z=0}}{\delta_z|_{B_z}}\left.\frac{c_{f_z}}{2}\right|_{B_z=0}. \quad (40)$$

Applying Eq. (31) to the both sides of Eq. (40) and integration in the axial distance yield

$$\delta_z|_{B_z} = \sqrt{\frac{(1+B_z)(1+B_z/2)}{1+(13/11)B_z+(4/11)B_z^2}}\;\delta_z|_{B_z=0}. \quad (41)$$

By substituting Eq. (41) into Eq. (31) and approximating B_z in the range from 2 to 50, one obtains

$$\frac{c_{f_z}|_{B_z}}{c_{f_z}|_{B_z=0}} = \frac{1}{1+B_z/2}\sqrt{\frac{1+(13/11)B_z+(4/11)B_z^2}{(1+B_z)(1+B_z/2)}} \approx q' B_z^{-k'} \tag{42}$$

where $(q', k') = (0.7275, 0.965)$.

Combining Eq. (33) with Eqs. (34), (36), and (42), one can evaluate the axial skin-friction coefficient as

$$\left.\frac{c_{f_z}}{2}\right|_{B_z} = \left(\frac{\alpha_z}{\beta_z}\,\xi_0\,\frac{\exp(\overline{p}\,\overline{z})-1}{\overline{p}\,\overline{z}}+1\right)^{1/(1-\gamma_z)} \times \left(\frac{\alpha_z}{\beta_z}\,\xi_0\exp(\overline{p}\,\overline{z})+1\right) q' B_z^{-k'}\cdot 0.03\mathrm{Re}_z^{-0.2}\,. \tag{43}$$

3.6 Derivation of Regression Rates in Swirl Injection Engines

In the previous subsection, the axial skin-friction coefficient was derived for conditions with swirl and fuel blowing as Eq. (41). The aim of this subsection is to obtain the heat flux to the wall and the regression rates in swirl hybrids. Now, substituting Eq. (6) into Eq. (43) yields

$$\dot{Q}_c = (0.03q')^{1/(1-k')}\,\rho_f^{-k'/(1-k')}\Delta h\,\frac{u_{z_e}}{u_{z_b}}\left(\frac{z}{\mu}\right)^{-0.2/(1-k')} \times \left(1+\frac{\alpha_z}{\beta_z}\,\xi_0\,\frac{\exp(pz)-1}{pz}\right)^{\gamma_z/((1-\gamma_z)(1-k'))} \left\{1+\frac{\alpha_z}{\beta_z}\,\xi_0\exp(pz)\right\}^{1/(1-k')} \times G_{zo}^{0.8/(1-k')}\dot{r}^{-k'/(1-k')} \tag{44}$$

where B_z has been eliminated with the definition of B_z and Eq. (43).

Substituting Eq. (44) into Eq. (1) yields

$$\dot{r} = \left(1+\frac{\alpha_z}{\beta_z}\,\xi_0\,\frac{\exp(pz)-1}{pz}\right)^{\gamma_z/(1-\gamma_z)} \times \left\{1+\frac{\alpha_z}{\beta_z}\,\xi_0\exp(pz)\right\} 0.03q'\left(\frac{z}{\mu}\right)^{-0.2}\rho_f^{-1}B_t^{1-k'}G_{zo}^{0.8} \tag{45}$$

where the definition of B_t is

$$B_t \equiv \frac{u_{e_z}\Delta h}{u_{b_z}h_\nu}$$

and B_t is equivalent to B_z at quasi-steady states because of Eqs. (1) and (6). Because B_t is a function of the thermochemical properties and O/F [12] when O/F is constant, B_t is constant in axial and radial directions. This is the reason why B_θ is considered as a variable and B_z as a constant.

According to the results by Marxman *et al.* [12], the heat flux to the wall can be expressed as follows:

$$\dot{Q}_c = (0.03q)^{1/(1-k)} \rho_f^{-k/(1-k)} \Delta h \, \frac{u_e}{u_b} \left(\frac{z}{\mu}\right)^{-0.2/(1-k)} G_o^{0.8/(1-k)} \dot{r}^{-k/(1-k)} \,. \quad (46)$$

Therefore, Eqs. (1) and (46) yield

$$\dot{r} = 0.03q \left(\frac{z}{\mu}\right)^{-0.2} \rho_f^{-1} B_t^{1-k} G_o^{0.8} \,. \quad (47)$$

Note that the experimental law for the regression rate is as follows:

$$\dot{r} = a \; G_o^n \,. \quad (48)$$

According to Karabeyoglu's theory [15], in axial flows, averaging of Eq. (47) in axial direction is equivalent to Eq. (48) and the exponent 0.8 at G_o in Eq. (47) should correspond to the exponent n at G_o in Eq. (48). On the basis of these findings, the coefficient a in Eq. (48) should be

$$a_0 = 0.03q \left(\frac{z}{\mu}\right)^{-0.2} \rho_f^{-1} B_t^{1-k} \quad (49)$$

where a is replaced by a_0 and $(q, k) = (1.2,\ 0.77)$ [6]. Then, in the same way as in Eq. (49), a in Eq. (45) should be equal to

$$a_\xi = \left(1 + \frac{\alpha_z}{\beta_z} \, \xi_0 \, \frac{\exp(pz) - 1}{pz}\right)^{\gamma_z/(1-\gamma_z)} \times \left\{1 + \frac{\alpha_z}{\beta_z} \, \xi_0 \exp(pz)\right\} 0.03q' \left(\frac{z}{\mu}\right)^{-0.2} \rho_f^{-1} B_t^{1-k'}$$

where a is replaced by a_ξ. These two coefficients show how the regression rates rise with the initial swirl strength ξ_0:

$$\frac{\dot{r}_\xi}{\dot{r}_0} = \frac{a_\xi}{a_0} = \left(1 + \frac{\alpha_z}{\beta_z} \, \xi_0 \, \frac{\exp(pz) - 1}{pz}\right)^{\gamma_z/(1-\gamma_z)} \left\{1 + \frac{\alpha_z}{\beta_z} \, \xi_0 \exp(pz)\right\} \frac{q'}{q} \, B_t^{k-k'} \,. \quad (50)$$

Thus, the heat flux to the wall and regression rates in swirl flows have been estimated.

4 COMPARISON OF THE REGRESSION RATES OF SWIRL ENGINES WITH EXPERIMENTS

In order to validate the model, one can compare the increase of the regression rate by swirl predicted by Eq. (50) and obtained in experiments by Yuasa *et al.* [3]. In this section, the prediction of Eq. (50) will be compared with the experiments in two ways. One of them is the comparison between the representative regression rates in the axial direction with space averaged values of the experimental results. Another one is the comparison of the axial distributions of regression rates.

4.1 Comparison of Representative and Averaged Regression Rates Along the Axial Direction

The fuel and oxidizer used in Yuasa's experiments are polymethylmethacrylate (PMMA) and gaseous oxygen. For PMMA [16], $B_t = 10$ and $\mu = 5.0 \cdot 10^{-7}$ Pa·s were set. To compare the prediction with the averaged data, let us set the representative axial location in Eq. (50) as $L/2$. The geometric swirl numbers of the injectors are 0, 9.7, and 19.4 and the range of the oxidizer mass flux is from 10 to 70 kg/(m^{2}s). The case with the port length $L = 150$ mm is shown in Fig. 3 and that with $L = 500$ mm is shown in Fig. 4.

In Yuasa's experiments, they claimed it was too difficult to measure the actual swirl numbers in their motors and when they plotted the regression rates, they used a kind of index called geometric swirl number indicating the strength of the swirl. This index is determined only by the geometry of engines and injectors and

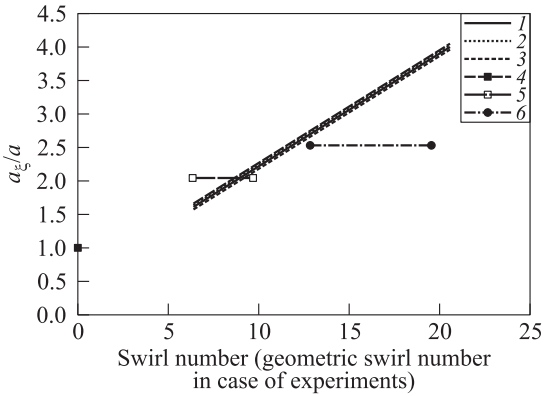

Figure 3 The ratio of constant a in swirl hybrid rocket engines for $L = 150$ mm: *1* — $G_o = 10$ kg/(m^{2}s); *2* — 15; *3* — $G_o = 20$ kg/(m^{2}s); *4* — experiment-1; *5* — experiment-2; and *6* — experiment-3

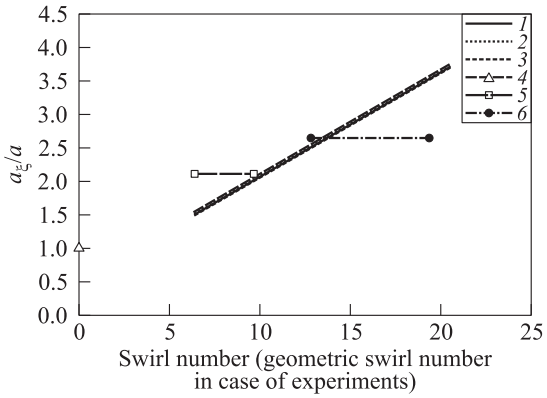

Figure 4 The ratio of constant a in swirl hybrid rocket engines for $L = 500$ mm: *1* — $G_o = 45$ kg/(m^{2}s); *2* — 50; *3* — $G_o = 55$ kg/(m^{2}s); *4* — experiment-1; *5* — experiment-2; and *6* — experiment-3

the authors think this number is not always equal to the actual swirl number. As a matter of fact, Motoe and Shimada [17] conducted numerical simulations of the swirl cold flow field where they used the shape or geometry of the chamber similar to Yuasa's. The calculated swirl numbers near the injectors were 0.66 in condition that the geometric swirl number was 5.5. For this reason, the present authors plotted the regression rate in Yuasa's experiment with the error bar in the swirl number direction. The error bars have the range of 66% to 100% of the geometry swirl numbers.

Note that for both port lengths, at large swirl numbers, the increase in the regression rates is largely consistent with the experiments and the positive correlation between the initial swirl numbers and the increase in the regression rates also generally exist in the set of experimental results and in the present authors' predictions. In their past research, because the present authors assumed that the decay of swirl and the axial skin-friction are not affected by fuel blowing, the increase in the regression rate was estimated to be much larger than in the experiments [18]. In this paper, this assumption was reconsidered because it does not reflect the actual physical phenomena as the swirl decay is mainly caused by skin-friction at the wall and fuel blowing should strongly affect it. Then, the methods to evaluate the skin friction with fuel blowing have been newly considered and the approaches used in subsections 3.4 and 3.5 showed better results than the past one. Thus, the regression rates were successfully evaluated for the cases with strong swirl.

However, in the range of small swirl numbers under 3, the regression rates appeared to be less than 1. This seems to be caused by the adopted simplifications, in particular, by the assumption on the exponential decay of swirl in cold

flow and by separate consideration of the effects of swirl flow and fuel blowing on the skin-friction coefficient. However, when applying vortex injection to hybrids, the initial swirl numbers will be designed to increase the regression rate and, by authors' opinion, this estimation method will be useful.

4.2 Comparison of the Axial Distribution of Regression Rates

Next, let us compare the prediction of the local regression rates in the swirl injection hybrids with the experiments conducted by Yuasa *et al.* The geometric swirl numbers of the injectors are 0, 9.7, and 19.4 and the axial location where the local regression rates are measured is from 30 to 500 mm; the oxidizer mass flux is 56.9 kg/(m^{2}s).

Figure 5 compares the local regression rate for axial injection obtained by Eq. (47) and in the experiment. In the experimental data, while the local regression rate decreases from the front edge of the fuel port to the middle of the fuel port and increases towards the end, the predicted regression rate by Marxman's evaluation gradually decreases along the axial distance. Furthermore, the location where the prediction agrees with the experimental data is only around the local minimun position. In the present authors' opinion, this disagreement suggests that other effects which increase the regression rate such as radiation and the increase of the mass flux due to fuel blowing have to be considered.

In Fig. 6, the local regression rates predicted by Eq. (45) are compared with Yuasa's experiments for the swirl-injection hybrid mortors. Similar to the case of axial injection, while both predicted regression rates and experimental results are of the same order of magnitude for high swirl numbers, their values are not the same. As in the case of comparison of the averaged rates, especially, at low

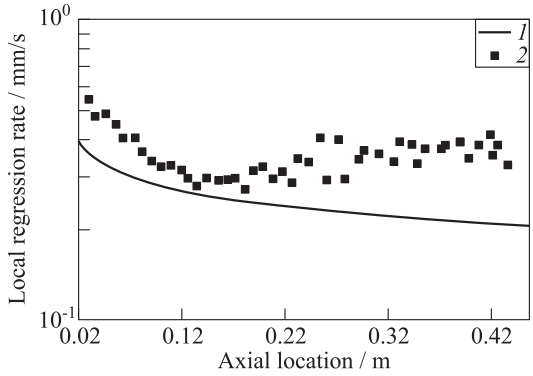

Figure 5 Comparison of the regression rates in axial hybrids between the Marxman's prediction method (*1*) and the Yuasa's experiment (*2*)

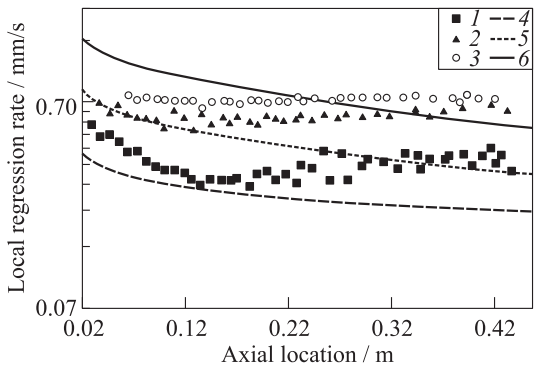

Figure 6 Comparison of the regression rates in swirl hybrids between the present theoretical prediction (curves) and the Yuasa's experiments (signs): *1* — $\xi_0 = 0$; *2* — 19.4; *3* — $\xi_0 = 38.8$; *4* — axial; *5* — $\xi_0 = 19.7 \cdot 0.66$; and *6* — $\xi_0 = 38.8 \cdot 0.66$

swirl numbers, the predictions differ considerably from the experimental data because Eq. (50) provides values under 1. Moreover, from Fig. 6, one can understand that even in the cases of axial injection where Marxman's model is thought to be applicable, the predictions of the regression rates do not agree with the experimental data and only the spatially averaged prediction agrees with the corresponding experimental data. However, according to Chiaverini *et al.* [11], the radiation effect is weakened by developing turbulence in boundary layers. In swirl flow, because streamlines near the wall are longer than in the axial flow, turbulence in the boundary layer is supposed to develop earlier and the effects of radiation should be low in swirl flow. Nevertheless, the discrepancy between theoretical and experimental regression rates does not become narrower for different swirl numbers. This consideration indicates that there exist a different mechanism of swirl number decline or the effects of fuel mass addition are large.

In view of it, before focusing on improving the evaluation of the effects caused by swirl injection, the present authors plan to use more accurate prediction models than the Marxman's classical one for predicting the distribution of local regression rates in axial flows which will consider the effect of the increase in the mass flow because of fuel vaporization.

As for the accuracy of estimating the effects of swirl, it is necessary to reconsider the relation of actual swirl numbers to the geometric ones. On the one hand, in the axial flow with swirl strength $\xi_0 = 19.4$, the predicted result is close to the experiment only around the front of fuel port; on the other hand, at $\xi_0 = 38.8$, the best agreement shifts to the middle of fuel port. In the authors' opinion, this is due to the fact that the swirl number of 0.66 is only applied to low swirl flows. In these studies, the swirl number of 0.66 has been used based

on the Motoe and Shimada numerical calculations [17]. However, this number is the result of condition that the geometric swirl number is 5.5 ($\xi_0 = 11$) and in higher swirl flows, the actual swirl numbers can decrease. In particular, in cases of high swirl strength, it is reasonable that this swirl number may not be used. Therefore, it is necessary to study the relation between actual and geometric swirl numbers.

5 CONCLUDING REMARKS

In this paper, the authors have theoretically reconstructed and extended Marxman's quasi-steady boundary layer combustion model and the prediction method for regression rates in swirling hybrid rocket motors. This has been made by extending the 2D flat-plate boundary layer theory to the 3D axisymmetric theory. The derived heat flux equation includes the effect of initial swirl strength and the swirl-strengthened fuel blocking effect. The blocking exponent for strong swirl injection is calculated to be 0.965 in contrast to 0.77 for axial injection. By using this heat flux, eventually, the equation to evaluate the regression rate in swirling hybrid rocket motors has been derived.

To confirm the accuracy of this method, the predicted results were compared with the experiments by Yuasa *et al.* in two ways. In the first, the representative increase of the regression rates by swirl in the axial direction were compared with the averaged regression rates from the experiments. Though the assumed flow field seems to be different from the experiments to some extent, the estimated regression rates are of the same order of magnitude at all swirl strengths and fit especially well at strong swirls. In the second, the predicted local regression rates were compared with experimental data from Yuasa *et al.* for both axial and swirl flows. The prediction of the classical Marxman's theory for axial injection motors was compared with the data for axial flow and the results were of the same order of magnitude, however, not accurate enough to claim the regression rates can be predicted to know the detailed performance. In the authors' opinion, the reason for this disagreement is that other effects which increase regression rates such as radiation and the increase of the mass flux by fuel blowing or other mechanisms inherent in swirl injection hybrid rocket engines have to be considered, though the radiation effect can be weakened at high swirl numbers. In swirl injection, because the theory derived in this paper is based on the classical theory of Marxman *et al.*, the accuracy of the prediction is also low. Therefore, to improve the prediction of the local regression rates in swirl injection hybrid motors, one should provide some theoretical correction of Marxman's boundary layer combustion model. Compared with experimental results, the predicted regression rates of $\xi_0 = 38.8$ were found to shift higher than the ones at low swirl num-

bers. This is because the relation of actual swirl numbers to the geometric ones can decrease due to the increase of geometric swirl numbers and it is necessary to reconsider the value of this relation at higher geometric swirl numbers.

ACKNOWLEDGMENTS

This research is supported by the Hybrid Rocket Research Working Group (HRrWG) of the Institute of Space and Astronautical Science, Japan Aerospace Exploration Agency. The authors thank the members of HRrWG for their helpful discussion.

REFERENCES

1. Zilliac, G., and M. A. Karabeyoglu. 2006. Hybrid rocket fuel regression rate data and modeling. AIAA Paper No. 2006-4504.
2. Knuth, W. H., M. J. Chiaverini, J. A. Sauer, and D. J. Gramer. 1998. Solid-fuel regression rate behavior of vortex hybrid rocket engines. *J. Propul. Power* 18:600–609.
3. Yuasa, S., K. Yamamoto, H. Hachiya, K. Kitagawa, and Y. Oowada. 2001. Development of a small sounding hybrid rocket with a swirling-oxidizer-type engine. AIAA Paper No. 2001-3537.
4. Yoshizawa, A., H. Abe, H. Fujiwara, Y. Mizobuchi, and Y. Matsuo. 2009. Reynolds-averaged modeling of turbulent-diffusion suppression mechanism in a swirling flow. *41st Fluid Dynamics Conference / Aerospace Numerical Simulation Symposium Proceedings*. 23–26.
5. Marxman, G. A., and M. Gilbert. 1963. Turbulent boundary layer combustion in the hybrid rocket. *Symposium (International) on Combustion Proceedings*. 9:371–383.
6. Marxman, G. A. 1965. Combustion in the turbulent boundary layer on a vaporing surface. *Symposium (International) on Combustion Proceedings*. 10: 1337–1349.
7. Lees, L. 1958. Convective heat transfer with mass addition and chemical reactions. *3rd AGARD Combustion and Propulsion Colloquium Proceedings*. 451.
8. Kito. M., H. Fujiwara, and K. Nakabayashi. 1985. The direct measurement of the shear stresses in swirl pipe flows. *Trans. Japan Soc. Mech. Eng. B* 51:2597–2605.
9. Steenbergen, W. 1995. Turbulent pipe flow with swirl. University Eindhoven of Technology. Ph.D. Thesis.
10. Karabeyoglu, M. A., and D. Altman. 1997. Transient behavior in hybrid rockets. AIAA Paper No. 97-2937.

11. Chiaverini, M. J., N. Serin, D. K. Johnson, Y.-C. Lu, K. K. Kuo, and G. A. Risha. 2000. Regression rate behavior of hybrid rocket solid fuels. *J. Propul. Power* 16:125–132.
12. Marxman, G. A., C. E. Wooldridge, and R. J. Muzzy. 1963. Fundamentals of hybrid boundary layer combustion. AIAA Paper No. 63-505.
13. Czernuszenko, W., and A. A. Rylov. 2000. A generalization of Prandtl's model for 3D open channel flows. *J. Hydraul. Res.* 38:173–383.
14. Dorrance, W. H., and F. J. Dore. 1954. The effect of mass transfer on the compressible turbulent boundary-layer skin friction and heat transfer. *J. Aeronaut. Sci.* 21:404–410.
15. Karabeyoglu, M. A., and D. Altman. 1999. Dynamic modeling of hybrid rocket combustion. *J. Propul. Power* 15:562–571.
16. Marxman, G. A. 1967. Boundary-layer combustion in propulsion. *Symposium (International) on Combustion Proceedings*. 11:269–289.
17. Motoe, M., and T. Shimada. 2009. Head-end injected swirling gas flow in a chamber. AIAA Paper. 2009-5025.
18. Ozawa, K., and T. Shimada. 2013. A theoretical study in the skin-friction coefficient in swirl pipe flows. *ISAS Proceedings of Space Propulsion Symposium FY2012. STCP-2012-070.* (In Japanese.)